



1 **Exploring the role of the “Ice-Ocean governor” and mesoscale eddies in the**

2 **equilibration of the Beaufort Gyre: lessons from observations**

3 Gianluca Meneghello *, Edward Doddridge, John Marshall, Jeffery Scott, Jean-Michel Campin

4 *Department of Earth, Atmospheric and Planetary Sciences, Massachusetts Institute of*

5 *Technology, Cambridge, Massachusetts 02139-4307, USA.*

6 *Corresponding author address: Department of Earth, Atmospheric and Planetary Sciences, Mas-
7 sachusetts Institute of Technology, Cambridge, Massachusetts 02139-4307, USA.

8 E-mail: gianluca.meneghello@gmail.com

Early Online Release: This preliminary version has been accepted for publication in *Journal of the Physical Oceanography*, may be fully cited, and has been assigned DOI 10.1175/JPO-D-18-0223.1. The final typeset copyedited article will replace the EOR at the above DOI when it is published.

ABSTRACT

9 Observations of Ekman pumping, sea surface height anomaly, and isohaline
10 depth anomaly over the Beaufort Gyre are used to explore the relative impor-
11 tance and role of (i) feedbacks between ice and ocean currents, dubbed the
12 “Ice-Ocean governor” and (ii) mesoscale eddy processes in the equilibration
13 of the Beaufort Gyre. A two-layer model of the gyre is fit to observations
14 and used to explore the mechanisms governing the gyre evolution from the
15 monthly to the decennial time scale. The Ice-Ocean governor dominates the
16 response on inter-annual timescales, with eddy processes becoming evident
17 only on the longest, decadal timescales.

18 **1. Introduction**

19 The Arctic Ocean's Beaufort Gyre, centered in the Canada Basin, is a large-scale, wind-driven,
20 anticyclonic circulation pattern characterized by a strong halocline stratification with relatively
21 fresh surface waters overlying saltier (and warmer) waters of Atlantic Ocean origin. The halo-
22 cline stratification inhibits the vertical flux of ocean heat to the overlying sea ice cover. Ekman
23 pumping associated with a persistent but highly variable Arctic high pressure system (Proshutin-
24 sky and Johnson 1997; Proshutinsky et al. 2009, 2015; Giles et al. 2012) accumulates freshwater
25 and inflates isopycnals. The induced isopycnal slope drives a geostrophically balanced flow whose
26 imprint can be clearly seen in the doming of sea surface height at the center of the Beaufort Sea
27 (see Figure 1).

28 Recent observational studies by Meneghello et al. (2017, 2018b); Dewey et al. (2018); Zhong
29 et al. (2018), have outlined how the interaction between the ice and the surface current plays a
30 central role in the equilibration of the Beaufort Gyre's geostrophic current intensity and its fresh-
31 water content. Downwelling-favorable winds and ice motion inflate the gyre until the relative
32 velocity between the geostrophic current and the ice velocity is close to zero, at which point the
33 surface-stress-driven Ekman pumping is turned off, and the gyre inflation is halted. In Meneghello
34 et al. (2018a) we developed a theory describing this negative feedback between the ice drift and
35 the ocean currents. We called it the "ice-ocean governor" by analogy with mechanical governors
36 that regulate the speed of engines and other devices through dynamical feedbacks (Maxwell 1867;
37 Bennet 1993; Murray et al. 2018).

38 Another mechanism at work, studied by Davis et al. (2014); Manucharyan et al. (2016);
39 Manucharyan and Spall (2016); Meneghello et al. (2017), and mimicking the mechanism of equi-
40 libration hypothesized for the ACC by Marshall et al. (2002); Karsten et al. (2002), relies on eddy

41 fluxes to release freshwater accumulated by the persistent anticyclonic winds blowing over the
42 gyre. In this scenario, representing the case of ice in free-drift, or the case of an ice free gyre,
43 the Ice-Ocean governor does not operate and the gyre inflates until baroclinic instability is strong
44 enough to balance the freshwater input.

45 In this study, we start from observations and address how both mechanisms interact in a real-
46 world Arctic, where we expect their role to change over the seasonal cycle as ice cover and ice
47 mobility vary. A theory for their combined role in the equilibration of the Beaufort Gyre has
48 been recently proposed by Doddridge et al. (2019). Here we begin by assimilating time series of
49 Ekman pumping, inferred from observations (see Meneghello et al. 2018b), and sea surface height,
50 obtained from satellite measurements (Armitage et al. 2016, see Figure 1a) into a two-layer model
51 of the Beaufort Gyre (see Figure 2). Despite its limitations, as we shall see our model is able to
52 capture much of the observed variability of the gyre. We then evaluate the relative role of the
53 Ice-Ocean governor and eddy fluxes in equilibrating the gyre's isopycnal depth anomaly, and its
54 freshwater content. We conclude by using these new insights to discuss how changes in the Arctic
55 ice cover will impact the state of the Beaufort gyre.

56 **2. Two-layer model of the Beaufort Gyre**

57 Let us consider a two-layer model comprising the sea surface height η and isopycnal depth
58 anomaly a , as shown in Figure 2 (see Section 12.4 of Cushman-Roisin and Beckers 2010). For
59 time scales T longer than one day ($Ro_T = \frac{1}{fT} < 0.1$, where $f = 1.45 \times 10^{-4} \text{ s}^{-1}$ is the Coriolis
60 parameter, and is assumed constant) and length scales L larger than 5 km ($Ro = \frac{U}{fL} < 0.1$, where
61 $U \approx 5 \text{ cm s}^{-1}$ is a characteristic velocity), currents in the interior of the Beaufort Gyre can be
62 considered in geostrophic balance everywhere except at the very top and bottom of the water
63 column, where frictional effects drive a divergent Ekman transport. The dynamics of the sea

64 surface height and isopycnal depth anomalies can then be approximated by

$$\begin{aligned} \frac{d(\eta - a)}{dt} &= K \frac{a}{L^2} - \underbrace{\bar{w}_{Ek}}_{\text{Top Ekman}} \\ \frac{da}{dt} &= -K \frac{a}{L^2} + \underbrace{\frac{d}{2f} \frac{g\eta + g'a}{L^2}}_{\text{Bottom Ekman}}, \end{aligned} \quad (1)$$

65 where $\frac{1}{L^2}$ represent a scaling for the laplacian operator (see Appendix A1 for a detailed derivation
 66 of (1)). Volume is gathered and released by the surface Ekman pumping $\bar{w}_{Ek} = \frac{1}{A} \int_A \frac{\nabla \times \tau}{\rho f} dA$,
 67 proportional to the curl of the surface stress τ , and by the bottom Ekman pumping $-\frac{d}{2f} \frac{g\eta + g'a}{L^2}$,
 68 proportional to the Ekman layer length scale d and driven by the bottom geostrophic current $\frac{\hat{k}}{f} \times$
 69 $\nabla(g\eta + g'a)$ (see Section 8.4 of Cushman-Roisin and Beckers 2010). The term $K \frac{a}{L^2}$ represents
 70 mesoscale eddies acting to flatten density surfaces. Vertical diffusivity is relatively low in the
 71 Arctic and, for simplicity, it is neglected in our model.

72 The reference water density is taken as $\rho = 1028 \text{ kg m}^{-3}$, and g and $g' = \frac{\Delta\rho}{\rho} g$ are the gravity and
 73 reduced gravity constants, with $\Delta\rho$ the difference between the potential density at the surface and
 74 at depth.

75 For the purpose of our discussion we consider the surface stress τ , to have a wind-driven τ_a and
 76 an ice-driven τ_i component, weighted by the ice concentration α

$$\tau = (1 - \alpha) \underbrace{\rho_a C_{Da} |\mathbf{u}_a| \mathbf{u}_a}_{\tau_a} + \alpha \underbrace{\rho C_{Di} |\mathbf{u}_i - \mathbf{u}_g| (\mathbf{u}_i - \mathbf{u}_g)}_{\tau_i}, \quad (2)$$

77 where \mathbf{u}_a , \mathbf{u}_i and \mathbf{u}_g are the observed wind, ice and surface geostrophic current velocities respec-
 78 tively, $\rho_a = 1.25 \text{ kg m}^{-3}$ is the air density, and $C_{Da} = 0.00125$ and $C_{Di} = 0.0055$ are the air-ocean
 79 and ice-ocean drag coefficients. We note how the geostrophic surface currents \mathbf{u}_g act as a negative
 80 feedback on the ice-driven component (see Meneghello et al. 2018a).

81 To better understand the relative role of the winds, sea-ice, ocean geostrophic currents, and
 82 eddy diffusivity in the equilibration of the gyre, we additionally compute the contribution of the

83 geostrophic current to the ice stress as

$$\tau_{ig} = \tau_i - \tau_{i0}, \quad (3)$$

84 where τ_{i0} is the ice-ocean stress neglecting the geostrophic current, i.e., computed by setting
85 $\mathbf{u}_g = 0$ in (2). Accordingly, we define the Ekman pumping associated with each component as

$$\begin{aligned} w_a &= \frac{\nabla \times ((1 - \alpha)\tau_a)}{\rho f} & w_i &= \frac{\nabla \times (\alpha\tau_i)}{\rho f} \\ w_{i0} &= \frac{\nabla \times (\alpha\tau_{i0})}{\rho f} & w_{ig} &= \frac{\nabla \times (\alpha\tau_{ig})}{\rho f}, \end{aligned} \quad (4)$$

86 so that the total Ekman pumping can be written as

$$w_{Ek} = w_a + w_i = w_a + w_{i0} + w_{ig}. \quad (5)$$

87 We also note that the eddy flux term $K \frac{a}{L^2}$, having units of m year^{-1} , can be expressed as an
88 equivalent Ekman pumping and compared with the other Ekman velocities.

89 The dynamics in (1) then describe a “wind-driven” Beaufort Gyre where water masses ex-
90 changes are limited to Ekman processes at the top and bottom of the domain, with eddies re-
91 distributing volume internally.

92 An observationally-based estimate of the relative importance of the Ice-Ocean governor contri-
93 bution w_{ig} and the eddy fluxes contribution $K \frac{a}{L^2}$ to the equilibration of the Beaufort Gyre is the
94 main focus of our study.

95 **3. Fitting parameters of the two-layer model using observations of the Beaufort Gyre**

96 In order to estimate the key parameters, we drive the model (1) using observed Ekman pumping
97 \bar{w}_{Ek} , averaged monthly and over the Beaufort Gyre Region (BGR, see Figure 1), and shown as a
98 black curve in Figure 3a.

99 Based on observational evidence (see, e.g., Figure 1 of Meneghello et al. (2018b)), we use $L =$
100 300km as the characteristic length scale over which derivatives of the ice, wind and geostrophic

101 current velocities should be computed. The monthly resolution of the dataset, and the chosen
102 length scale of interest, results in a temporal Rossby number $Ro_T \approx 3 \times 10^{-3}$ and a Rossby number
103 $Ro \approx 1 \times 10^{-3}$: the geostrophic approximation behind the derivation of our model (1) are then
104 verified, and the quasi-geostrophic correction is negligible (see also Appendix A1).

105 We then vary K , g' , and d , as well as the initial conditions of sea surface height and isopycnal
106 depth anomalies, to minimize the departure of the estimated sea surface height anomaly from the
107 observed one, shown as a black curve in Figure 3b. The data used are described in Appendix A2.
108 The procedure to estimate the 5 free parameters using the 144 monthly observational data points
109 is outlined in Appendix A3.

110 The estimated sea surface height anomaly (Figure 3b, blue) closely follows the observed one
111 (black) (RMSE = 0.02 m, $R^2 = 0.68$) and captures relatively well both the seasonal cycle and the
112 relatively sudden changes in sea surface height and isopycnal depth anomaly that occurred in 2007
113 and 2012, both associated with changes in the ice extent and atmospheric circulation (McPhee et al.
114 2009; Simmonds and Rudeva 2012). Red squares mark the observed August September October
115 mean 30 psu isohaline depth anomaly, corresponding to the surface layer depth anomaly, and are
116 not used in the data estimation process.

117 The estimated parameters, and their standard deviations, are $K = (218 \pm 31) \text{ m}^2 \text{ s}^{-1}$ and $g' =$
118 $(0.065 \pm 0.007) \text{ m s}^{-2}$ (or, equivalently, $\Delta\rho = 6.8 \text{ kg m}^{-3}$) broadly in accord with observations
119 (see Meneghello et al. 2017, and Figure 1b). The estimated bottom Ekman layer thickness
120 $d = (58 \pm 11) \text{ m}$ includes bathymetry effects which cannot be represented in our model.

121 We note that our parameter estimate depends on the choice of the length scale L , so that we will
122 use our estimates primarily to gain a physical intuition of the relative importance of the processes
123 at play. Nonetheless, the fact that such values are very close to observations suggests that the
124 choice of L is appropriate. More importantly, neither the captured variance R^2 — informing us

125 about the accuracy of the model — nor the analysis outlined in the next section depends on the
126 choice of the length scale L .

127 Our simple model estimates a single constant value of eddy diffusivity for the entire Beaufort
128 Gyre region. Previous work on the Beaufort Gyre has suggested that the eddy diffusivity vary
129 in space (Meneghello et al. 2017) and depends on the state of the large-scale flow and its history
130 (Manucharyan et al. 2016, 2017), while studies focussing on the Southern Ocean have shown
131 that eddy diffusivity varies in both space and time (Meredith and Hogg 2006; Wang and Stewart
132 2018). Similarly, in our computation of Ekman pumping (Meneghello et al. 2018b) we assume a
133 constant value for the drag coefficient despite the fact that observational evidence suggest a large
134 variability (Cole et al. 2017). Despite its limitations, our model is able to capture much of the
135 observed variability of the gyre over the time period considered, and will be used in the next
136 section to discuss the relative role of the governor and eddy fluxes in the gyre equilibration.

137 **4. Relative importance of the Ice-Ocean governor and eddy fluxes**

138 Now that parameters of our model (1) have been estimated using available observations, we
139 can analyze the different role of each term in the equilibration of the Beaufort Gyre. Figure 4a
140 shows monthly running means of wind-driven w_a and ice-driven w_{i0} downwelling favorable Ek-
141 man pumping (cumulative mean of $-12.2 \text{ m year}^{-1}$, dark and light blue respectively). This is
142 to be compared with the deflating effect of eddy fluxes $K \frac{a}{L^2}$ (equivalent to a mean upwelling of
143 1.8 m year^{-1} , dark red) and of the upwelling favorable Ice-Ocean governor Ekman pumping w_{ig}
144 (mean of 9.8 m year^{-1} upwards, light red). Over the 12 years of the available data, the contribu-
145 tion of the governor, reducing freshwater accumulation by limiting, or at time reversing, Ekman
146 downwelling, is six times larger than the freshwater release associated with eddy fluxes. The

147 small residual Ekman pumping of -0.6 m year^{-1} accounts for the 7 m increase in isopycnal depth
148 between 2003 and 2014 (red line in Figure 3b), consistent with observations.

149 The Ice-Ocean governor, acting on both barotropic (fast) and baroclinic (slower) timescales,
150 plays a much larger role than that of eddy fluxes. As can be seen from Figure 4, the upwelling effect
151 of the Ice-Ocean governor (light red) closely mirrors the downwelling effect of the ice motion
152 (light blue), both having important variations over the seasonal cycle, and essentially canceling the
153 net Ekman pumping within the ice covered regions of the gyre. In contrast, eddy fluxes provide
154 a much smaller, but persistent, mechanism releasing the accumulated freshwater and flattening
155 isopycnals.

156 To gain further insights into the different role played by the two mechanisms in the equilibration
157 of the gyre, we show in Figure 4b the hypothetical evolution of the isopycnal depth anomaly
158 when neglecting eddy fluxes (orange) and when neglecting the Ice-Ocean governor (i.e., setting
159 $w_{Ek} = w_a + w_{i0}$), while keeping the eddy diffusivity unchanged at $K = 218 \text{ m}^2 \text{ s}^{-1}$ (blue). In both
160 cases, we integrate the gyre model (1) using daily values of Ekman pumping (Meneghello et al.
161 2018b), starting from the same sea surface height and isopycnal depth anomaly on January 1st,
162 2003. It is clear how the isopycnal depth anomaly change between 2003 and 2014, estimated in
163 the absence of the ice-ocean governor and with realistic values of eddy diffusivity, would have
164 been more than 10 times the actual value of 7 m, while the error introduced by neglecting the eddy
165 diffusivity would be smaller.

166 It is of course possible to consider a scenario in which the dominating balance is the one between
167 Ekman pumping and eddy fluxes, as suggested by, e.g., Davis et al. (2014); Manucharyan and Spall
168 (2016). Such scenario can be tested by neglecting the feedback of the geostrophic current w_{ig} from
169 the Ekman pumping (see equation (5)) and estimating the eddy fluxes after fixing the stratification
170 to a realistic value of 6.8 kg m^{-3} . The resulting eddy diffusivity is $(1519 \pm 281) \text{ m}^2 \text{ s}^{-1}$, while the

171 bottom Ekman layer depth $d = (90 \pm 47)$ m. Such value of eddy diffusivity is more typical of the
172 Southern Ocean than the Arctic.

173 **5. Conclusions**

174 Using observational estimates of Ekman pumping (Meneghello et al. 2017) and sea surface
175 height anomaly (Armitage et al. 2016) we have estimated key parameters of a two layer model,
176 and studied the relative effect of eddy fluxes and of the Ice-Ocean governor on the equilibration of
177 the Beaufort Gyre. Both mechanisms have been previously addressed separately in both theoretical
178 and observational settings by Davis et al. (2014); Manucharyan et al. (2016); Manucharyan and
179 Spall (2016); Meneghello et al. (2017) and by Meneghello et al. (2018a,b); Dewey et al. (2018);
180 Zhong et al. (2018); Kwok et al. (2013). A theoretical framework unifying the two has been
181 detailed by Doddridge et al. (2019). Here, however, we have brought the two together in the
182 context of observations, and used those observations to explore the relative importance of the two
183 mechanisms.

184 In the current state of the Arctic, the Ice-Ocean governor plays a much more significant role
185 than eddy fluxes in regulating the gyre intensity and its freshwater content. As can be inferred
186 from Figure 4, this is particularly true on seasonal-to-interannual timescales. We judge that the
187 freshwater not accumulated (by reduced Ekman downwelling) or released (by Ekman upwelling)
188 by the Ice-Ocean governor is more than five times the freshwater released by eddies. This reminds
189 us of how central is the interaction of ice with the underlying ocean in setting the timescale of
190 response of the gyre and its ability to store fresh water. Moreover, this is a very difficult process to
191 capture in models because it demands that we faithfully represent internal lateral stresses within
192 the ice.

193 Future circulation regimes will be impacted by the changes in the concentration, thickness and
194 mobility of ice that have significantly evolved over the past two decades. In particular, loss of
195 multi-year ice and increased seasonality of the Arctic sea ice extent is to be expected, with sum-
196 mers characterized by ice-free or very mobile ice conditions, and winters characterized by an
197 extensive ice cover (Haine and Martin 2017). Depending on the internal strength of winter-ice, the
198 Arctic Ocean could evolve in the following two rather different scenarios. If the ice is very mobile
199 then the present seasonal cycle of upwelling and downwelling (red and blue shaded areas in Fig-
200 ure 3) would be replaced by persistent, year-long downwelling. This would result in an increase
201 in the depth of the halocline and more accumulation of fresh water. Ultimately the gyre would
202 be stabilized through expulsion of fresh water from the Beaufort Gyre via enhanced eddy activity.
203 However, if winter ice remains rigid, downwelling in the summer will be balanced by upwelling
204 in the winter as the anticyclonic gyre rubs up against the winter-ice cover; stronger geostrophic
205 currents will potentially result in stronger upwelling cycles, affecting the ocean stratification and
206 increasing the variability of the isopycnal depth, geostrophic current and freshwater content over
207 the seasonal cycle. Our ability to predict these changes depends on how well our models can rep-
208 resent the transfer of stress from the wind to the underlying ocean, through the seasonal cycle of
209 ice formation and melting.

210 *Acknowledgments.* The authors thankfully acknowledge support from NSF Polar Programs, both
211 Arctic and Antarctic, and the MIT-GISS collaborative agreement.

212

APPENDIX

213 **A1. Derivation of the governing equations**

214 Let us consider the volume conservation equations for a flat-bottom, two-layer model with layers
 215 thicknesses h_1 and h_2 and velocities \mathbf{u}_1 and \mathbf{u}_2 (see Section 12.4 of Cushman-Roisin and Beckers
 216 2010)

$$\begin{aligned}\frac{\partial h_1}{\partial t} + \nabla \cdot (h_1 \mathbf{u}_1) &= 0 \\ \frac{\partial h_2}{\partial t} + \nabla \cdot (h_2 \mathbf{u}_2) &= 0\end{aligned}\tag{A1}$$

217 In the hypothesis of low Rossby $Ro = \frac{U}{fL}$ and temporal Rossby $Ro_T = \frac{1}{fT}$ numbers, the accel-
 218 eration and advection terms in the momentum equations can be neglected and the velocity can be
 219 decomposed in a geostrophic $\mathbf{u}_{g1,g2}$ and an Ekman $\mathbf{u}_{e1,e2}$ component, so that for each layer

$$\mathbf{u} = \mathbf{u}_g + \mathbf{u}_e.\tag{A2}$$

220 The divergence free geostrophic component can be expressed as a function of the layer thick-
 221 nesses as

$$\begin{aligned}\mathbf{u}_{g1} &= \frac{g}{f} \hat{\mathbf{k}} \times \nabla (h_1 + h_2) \\ \mathbf{u}_{g2} &= \frac{g}{f} \hat{\mathbf{k}} \times \nabla (h_1 + h_2) + \frac{g'}{f} \hat{\mathbf{k}} \times \nabla h_2\end{aligned}\tag{A3}$$

222 while the vertically integrated volume divergence of the Ekman components, limited to the very
 223 top and the very bottom of the two layers (see the gray areas Figure 2), can be expressed as a
 224 function of the surface stress $\boldsymbol{\tau}$ and the bottom pressure $p = g(h_1 + h_2) + g'h_2$ as

$$\begin{aligned}\nabla \cdot (h_1 \mathbf{u}_{e1}) &= -\frac{\nabla \times \boldsymbol{\tau}}{\rho f} \\ \nabla \cdot (h_2 \mathbf{u}_{e2}) &= \frac{d}{2\rho f} \nabla^2 (g(h_1 + h_2) + g'h_2)\end{aligned}\tag{A4}$$

225 Using (A4), (A3) and (A2) the volume conservation equations (A1) can be rewritten as

$$\begin{aligned} \frac{\partial h_1}{\partial t} - \frac{g}{f} (\hat{\mathbf{k}} \times \nabla h_1) \cdot \nabla h_2 - \frac{\nabla \times \boldsymbol{\tau}}{\rho f} &= 0 \\ \frac{\partial h_2}{\partial t} + \frac{g}{f} (\hat{\mathbf{k}} \times \nabla h_1) \cdot \nabla h_2 + \frac{d}{2\rho f} \nabla^2 (g(h_1 + h_2) + g'h_2) &= 0 \end{aligned} \quad (\text{A5})$$

226 By defining the mean layer thicknesses H_1 and H_2 , equation (A5) can be restated in terms of sea
227 surface height anomaly $\eta = h_1 + h_2 - (H_1 + H_2)$ and isopycnal depth anomaly $a = h_2 - H_2$

$$\begin{aligned} \frac{\partial \eta}{\partial t} + \underbrace{\frac{d}{2\rho f} \nabla^2 (g\eta + g'a)}_{\text{bottom Ekman flux}} - \underbrace{\frac{\nabla \times \boldsymbol{\tau}}{\rho f}}_{\text{top Ekman flux}} &= 0 \\ \frac{\partial a}{\partial t} + \underbrace{\frac{g}{f} (\hat{\mathbf{k}} \times \nabla \eta) \cdot \nabla a}_{\text{isopycnal advection}} + \underbrace{\frac{d}{2\rho f} \nabla^2 (g\eta + g'a)}_{\text{bottom Ekman flux}} &= 0 \end{aligned} \quad (\text{A6})$$

228 We remark that for typical values of $L \approx 100$ km, $\eta \approx 0.1$ m, $a \approx 10$ m, $g' \approx 0.1$ ms⁻², $d \approx 10$ m
229 and for a time scale of the order of a month, all terms are of order 10⁻⁵. The only exception is
230 the term $\frac{\partial \eta}{\partial t}$ which while negligible, is retained to avoid having to deal with an integro-differential
231 equation to assimilate the sea surface height η .

232 Using an eddy closure for the isopycnal advection term, we can write

$$\overline{\frac{g}{f} (\hat{\mathbf{k}} \times \nabla \eta') \cdot \nabla a'} = -K \nabla^2 a \quad (\text{A7})$$

233 where K is a diffusivity coefficient, η' and a' are perturbations and the mean $(\hat{\mathbf{k}} \times \nabla \bar{\eta}) \cdot \nabla \bar{a}$ is ne-
234 glected because, on long time scales, the sea surface height and isopycnal depth anomaly gradients
235 are parallel.

236 Substitution of (A7) in (A6), and the approximation $\nabla^2 = \frac{1}{L^2}$, gives equation (1).

237 A2. Data

238 In order to constrain the model (1), we use observational estimates of Ekman pumping \bar{w}_{Ek} and
239 sea surface height anomaly η (see Supplemental Material).

240 Ekman pumping is shown in Figure 3a, where blue and red shading denote downwelling and
241 upwelling time periods respectively. We remark how the presence of winter upwelling is a direct
242 consequence of the inclusion of the geostrophic current in our estimates, is in agreement with
243 results from Dewey et al. (2018) and Zhong et al. (2018), and lower than previous estimates by
244 Yang (2006, 2009). The monthly time series of Ekman pumping used in this work is obtained
245 by averaging our Arctic-wide observational estimates (Meneghello et al. 2017, 2018b) over the
246 Beaufort Gyre Region (BGR, see Figure 1), and are thus based on sea ice concentration α from
247 Nimbus-7 SMMR and DMSP SSM/I–SSMIS passive microwave data, version 1 (Cavaliere et al.
248 1996), sea ice velocity u_i from the Polar Pathfinder daily 25-km Equal-Area Scalable Earth Grid
249 (EASE-Grid) sea ice motion vectors, version 3 (Tschudi et al. 2016), geostrophic currents u_g
250 computed from dynamic ocean topography (Armitage et al. 2016, 2017), and 10-m wind u_a from
251 the NCEP–NCAR Reanalysis 1 (Kalnay et al. 1996).

252 The mean sea surface height anomaly, shown by a black line in Figure 3b, is computed as the
253 norm of the gradient of sea surface height estimates by Armitage et al. (2016), multiplied by
254 $L = 300$ km, a characteristic length scale for the wind and ice velocity gradients — see, e.g.,
255 Figure 1 of Meneghello et al. (2018b). The original sea surface height estimate is available on a
256 $0.75^\circ \times 0.25^\circ$ grid, and is obtained by combining Envisat (2003–2011) and CryoSat-2 (2012–2014)
257 observations of sea surface height from the open ocean and ice-covered ocean (via leads). A total
258 of 1761 grid points from the original dataset are used to compute the BGR-averaged sea surface
259 height anomaly for each month.

260 While not used to constrain the model, an estimate of the mean isohaline depth anomaly, shown
261 as red marks in Figure 3b, is obtained in a similar fashion. We start from the 50 km resolution
262 August–September–October 30 psu isohaline depth estimated using CTD, XCTD, and UCTD pro-
263 files collected each year from July through October, and available at <http://www.whoi.edu/>

264 page.do?pid=161756. The norm of the isohaline gradient is averaged over the BGR and mul-
265 tiplied by the reference length $L = 300$ km. A total of 409 grid points are used to compute the
266 BGR-averaged isohaline depth anomaly for each month.

267 **A3. Parameter estimation**

268 In this section we report the Matlab code for the parameter estimation. Table A1 is provided as
269 supplemental material.

```
270 % load Ekman pumping (we) and
271 % sea surface height (eta)
272 % from table A1
273 infile = readtable('tableA1.dat');
274 we      = infile.wemonthly;
275 eta     = infile.eta;
276
277 % time step is 1 month
278 dt      = 3600*24*365/12.;
279
280 % initialize Matlab data object
281 z       = iddata(eta,we,dt)
282
283 % initialize estimation options
284 greyopt = greystOptions;
285 greyopt.Focus = 'simulation';
286
287 % initialize Linear ODE model
```

```

288 % with identifiable parameters
289 % - K      : eddy diffusivity
290 % - d      : bottom Ekman layer depth
291 % - drho   : potential density anomaly
292 pars      = {'K',300;'d',100;'drho',6};
293 sysinit = idgrey('model',pars,'c');
294
295 % estimate parameters
296 [sys,x0] = greyest(z,sysinit,greyst);
297
298 % the linear ODE model (see equation 1)
299 function [A,B,C,D] = model(K,d,drho,Ts)
300 rho      = 1028.;          % reference density
301 f        = 1.45e-4;       % coriolis parameter
302 g        = 9.81;          % gravity constant
303 gp       = g*drho/rho;    % reduced gravity
304 L        = 300000.;       % reference radius
305 c1       = d/(2*f)/L^2;
306
307 A = [ -c1*g ,   c1*gp           ;
308       +c1*g , -c1*gp - K/L^2 ];
309 B = [-1 ; 0];
310 C = [ 1 , 0];
311 D = [ 0 ];
312 end

```


313 **References**

- 314 Armitage, T. W. K., S. Bacon, A. L. Ridout, A. A. Petty, S. Wolbach, and M. Tsamados, 2017:
315 Arctic Ocean geostrophic circulation 2003-2014. *The Cryosphere Discussions*, **2017**, 1–32, doi:
316 10.5194/tc-2017-22, URL <http://www.the-cryosphere-discuss.net/tc-2017-22/>.
- 317 Armitage, T. W. K., S. Bacon, A. L. Ridout, S. F. Thomas, Y. Aksenov, and D. J. Wing-
318 ham, 2016: Arctic sea surface height variability and change from satellite radar altimetry and
319 GRACE, 2003-2014. *Journal of Geophysical Research: Oceans*, **121** (6), 4303–4322, doi:
320 10.1002/2015JC011579.
- 321 Bennet, S., 1993: *A history of control engineering, 1930-1955*. IET, 262 pp., doi:10.1049/
322 PBCE047E.
- 323 Cavalieri, D. J., C. L. Parkinson, P. Gloersen, and H. J. Zwally, 1996: Sea Ice Concentrations
324 from Nimbus-7 SMMR and DMSP SSM/I-SSMIS Passive Microwave Data, Version 1. NASA
325 National Snow and Ice Data Center Distributed Active Archive Center, Boulder, Colorado USA,
326 doi:10.5067/8GQ8LZQVL0VL.
- 327 Cole, S. T., and Coauthors, 2017: Ice and ocean velocity in the Arctic marginal ice zone: Ice rough-
328 ness and momentum transfer. *Elementa: Science of the Anthropocene*, doi:10.1525/elementa.
329 241.
- 330 Cushman-Roisin, B., and J.-M. Beckers, 2010: *Introduction to Geophysical Fluid Dynamics.*
331 *Physical and Numerical Aspects*, Vol. 101. 786 pp., doi:10.1016/B978-0-12-088759-0.00022-5.
- 332 Davis, P., C. Lique, and H. L. Johnson, 2014: On the link between arctic sea ice decline and
333 the freshwater content of the beaufort gyre: Insights from a simple process model. *Journal of*
334 *Climate*, **27** (21), 8170–8184, doi:10.1175/JCLI-D-14-00090.1.

335 Dewey, S., J. Morison, R. Kwok, S. Dickinson, D. Morison, and R. Andersen, 2018: Arctic Ice-
336 Ocean Coupling and Gyre Equilibration Observed With Remote Sensing. *Geophysical Research*
337 *Letters*, doi:10.1002/2017GL076229, URL <http://doi.wiley.com/10.1002/2017GL076229>.

338 Doddridge, E. W., G. Meneghello, J. Marshall, J. Scott, and C. Lique, 2019: A Three-way Balance
339 in The Beaufort Gyre: The Ice-Ocean Governor, Wind Stress, and Eddy Diffusivity. *J. Geophys.*
340 *Res. C: Oceans*, **124**, doi:10.1029/2018JC014897.

341 Giles, K. A., S. W. Laxon, A. L. Ridout, D. J. Wingham, and S. Bacon, 2012: Western Arc-
342 tic Ocean freshwater storage increased by wind-driven spin-up of the Beaufort Gyre. *Nature*
343 *Geoscience*, **5** (3), 194–197, doi:10.1038/ngeo1379, URL [http://www.nature.com/doifinder/10.](http://www.nature.com/doifinder/10.1038/ngeo1379)
344 [1038/ngeo1379](http://www.nature.com/doifinder/10.1038/ngeo1379).

345 Haine, T. W., and T. Martin, 2017: The Arctic-Subarctic sea ice system is entering a seasonal
346 regime: Implications for future Arctic amplification. *Scientific Reports*, **7** (1), 1–9, doi:10.1038/
347 [s41598-017-04573-0](https://doi.org/10.1038/s41598-017-04573-0).

348 Kalnay, E., and Coauthors, 1996: The NCEP/NCAR 40-year reanalysis project. *Bulletin of the*
349 *American Meteorological Society*, **77** (3), 437–471, doi:10.1175/1520-0477(1996)077<0437:
350 [TNYRP%2.0.CO;2](https://doi.org/10.1175/1520-0477(1996)077<0437:TNYRP%2.0.CO;2), arXiv:1011.1669v3.

351 Karsten, R., H. Jones, and J. Marshall, 2002: The Role of Eddy Transfer in Setting the Stratifica-
352 tion and Transport of a Circumpolar Current. *Journal of Physical Oceanography*, **32** (1), 39–54,
353 doi:10.1175/1520-0485(2002)032<0039:TROETI>2.0.CO;2.

354 Kwok, R., G. Spreen, and S. Pang, 2013: Arctic sea ice circulation and drift speed: Decadal
355 trends and ocean currents. *Journal of Geophysical Research: Oceans*, **118** (5), 2408–2425, doi:
356 [10.1002/jgrc.20191](https://doi.org/10.1002/jgrc.20191).

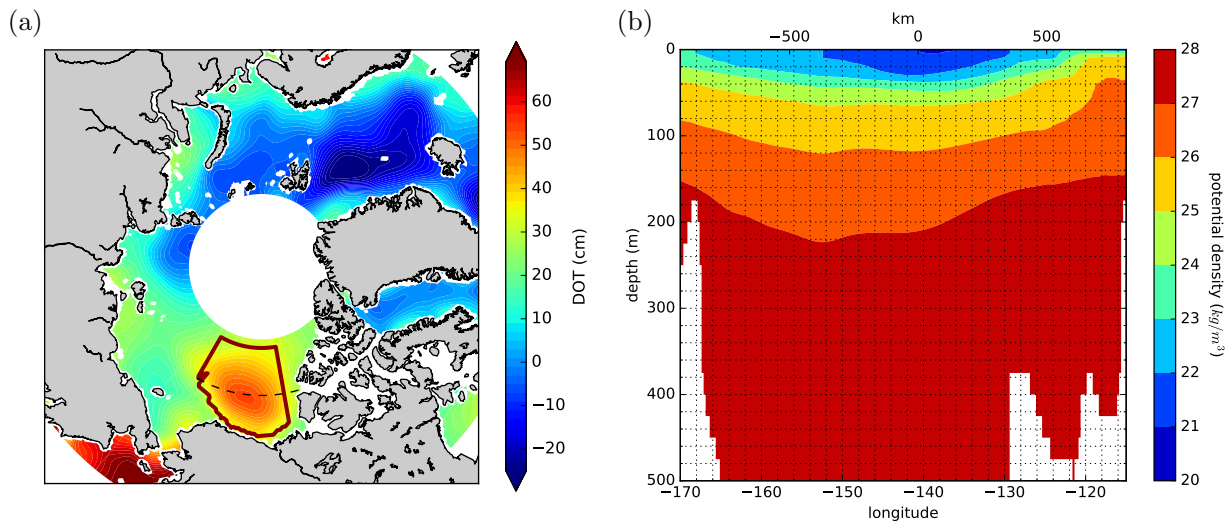
- 357 Manucharyan, G. E., and M. A. Spall, 2016: Wind-driven freshwater buildup and release in the
358 Beaufort Gyre constrained by mesoscale eddies. *Geophysical Research Letters*, **43** (1), 273–
359 282, doi:10.1002/2015GL065957.
- 360 Manucharyan, G. E., M. A. Spall, and A. F. Thompson, 2016: A Theory of the Wind-Driven
361 Beaufort Gyre Variability. *Journal of Physical Oceanography*, (2013), 3263–3278, doi:10.
362 1175/JPO-D-16-0091.1.
- 363 Manucharyan, G. E., A. F. Thompson, and M. A. Spall, 2017: Eddy Memory Mode of Mul-
364 tidecadal Variability in Residual-Mean Ocean Circulations with Application to the Beaufort
365 Gyre. *Journal of Physical Oceanography*, **47** (4), 855–866, doi:10.1175/JPO-D-16-0194.1,
366 URL <http://journals.ametsoc.org/doi/10.1175/JPO-D-16-0194.1>.
- 367 Marshall, J., H. Jones, R. Karsten, and R. Wardle, 2002: Can Eddies Set Ocean Stratification?
368 *Journal of Physical Oceanography*, **32** (1), 26–38, doi:10.1175/1520-0485(2002)032<0026:
369 CESOS>2.0.CO;2, URL [http://dx.doi.org/10.1175/1520-0485\(2002\)032{\%}3C0026:](http://dx.doi.org/10.1175/1520-0485(2002)032{\%}3C0026:)
370 [CESOS{\%}3E2.0.CO{\%}5Cn2](http://dx.doi.org/10.1175/1520-0485(2002)032{\%}3C0026:CESOS{\%}3E2.0.CO{\%}5Cn2).
- 371 Maxwell, J. C., 1867: On Governors. *Proceedings of the Royal Society of London*, **16**, 270–283,
372 doi:10.1098/rspl.1867.0055.
- 373 McPhee, M. G., A. Proshutinsky, J. H. Morison, M. Steele, and M. B. Alkire, 2009: Rapid change
374 in freshwater content of the Arctic Ocean. *Geophysical Research Letters*, **36** (10), 1–6, doi:
375 10.1029/2009GL037525.
- 376 Meneghello, G., J. Marshall, S. T. Cole, and M.-L. Timmermans, 2017: Observational inferences
377 of lateral eddy diffusivity in the halocline of the Beaufort Gyre. *Geophysical Research Letters*,
378 **44**, 1–8, doi:10.1002/2017GL075126, URL <http://doi.wiley.com/10.1002/2017GL075126>.

- 379 Meneghello, G., J. Marshall, M.-l. Timmermans, J.-m. Campin, and E. Doddridge, 2018a: The Ice-
380 Ocean Governor : Ice-Ocean Stress Feedback Limits Beaufort Gyre Spin-Up Special Section :.
381 1–7, doi:10.1029/2018GL080171.
- 382 Meneghello, G., J. Marshall, M.-L. Timmermans, and J. Scott, 2018b: Observations of sea-
383 sonal upwelling and downwelling in the Beaufort Sea mediated by sea ice. *Journal of Physical*
384 *Oceanography*, **48**, 795–805, doi:10.1175/JPO-D-17-0188.1.
- 385 Meredith, M. P., and A. M. Hogg, 2006: Circumpolar response of Southern Ocean eddy activ-
386 ity to a change in the Southern Annular Mode. *Geophysical Research Letters*, doi:10.1029/
387 2006GL026499.
- 388 Murray, J., H. Bradley, W. Craigie, C. T. Onions, R. Burchfield, E. WEiner, and J. Simpson, 2018:
389 governor. *The Oxford English Dictionary*, Oxford University Press.
- 390 Proshutinsky, A., D. Dukhovskoy, M.-l. Timmermans, R. Krishfield, and J. L. Bamber, 2015:
391 Arctic circulation regimes. *Philosophical transactions. Series A, Mathematical, physical, and*
392 *engineering sciences*, **373 (2052)**, 20140 160, doi:10.1098/rsta.2014.0160, URL [http://rsta.](http://rsta.royalsocietypublishing.org/content/373/2052/20140160)
393 [royalsocietypublishing.org/content/373/2052/20140160](http://rsta.royalsocietypublishing.org/content/373/2052/20140160).
- 394 Proshutinsky, A., and M. A. Johnson, 1997: Two circulation regimes of the wind-driven Arc-
395 tic Ocean. *Journal of Geophysical Research: Oceans*, **102 (C6)**, 12 493–12 514, doi:10.1029/
396 97JC00738.
- 397 Proshutinsky, A., and Coauthors, 2009: Beaufort Gyre freshwater reservoir : State and variability
398 from observations. *Journal of Geophysical Research*, **114**, 1–25, doi:10.1029/2008JC005104.
- 399 Simmonds, I., and I. Rudeva, 2012: The great Arctic cyclone of August 2012. *Geophysical Re-*
400 *search Letters*, **39 (23)**, 1–6, doi:10.1029/2012GL054259.

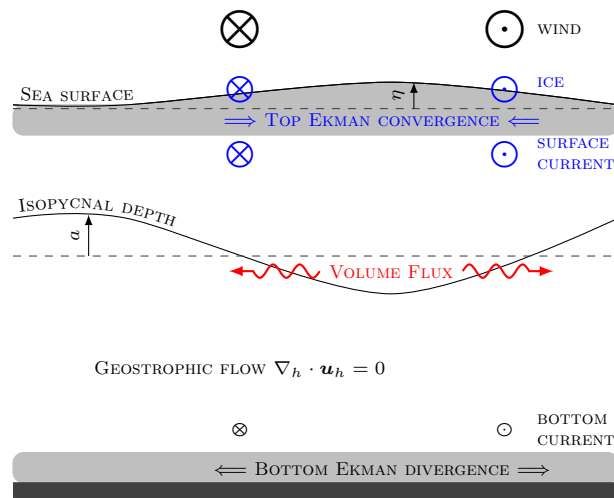
- 401 Tschudi, M., C. Fowler, J. S. Maslanik, and W. Meier, 2016: Polar Pathfinder Daily 25 km EASE-
402 Grid Sea Ice Motion Vectors, Version 3. URL <http://dx.doi.org/10.5067/O57VAIT2AYYY>, doi:
403 10.5067/O57VAIT2AYYY.
- 404 Wang, Y., and A. L. Stewart, 2018: Eddy dynamics over continental slopes under retrograde winds:
405 Insights from a model inter-comparison. *Ocean Modelling*, doi:10.1016/j.ocemod.2017.11.006,
406 arXiv:1011.1669v3.
- 407 Yang, J., 2006: The seasonal variability of the Arctic Ocean Ekman transport and its role in
408 the mixed layer heat and salt fluxes. *Journal of Climate*, **19** (20), 5366–5387, doi:10.1175/
409 JCLI3892.1.
- 410 Yang, J., 2009: Seasonal and interannual variability of downwelling in the Beaufort Sea.
411 *J Geophys Res*, **114**, C00A14, doi:10.1029/2008JC005084, URL [http://dx.doi.org/10.1029/
412 2008JC005084](http://dx.doi.org/10.1029/2008JC005084).
- 413 Zhong, W., M. Steele, J. Zhang, and J. Zhao, 2018: Greater Role of Geostrophic Currents in
414 Ekman Dynamics in the Western Arctic Ocean as a Mechanism for Beaufort Gyre Stabilization.
415 *Journal of Geophysical Research: Oceans*, doi:10.1002/2017JC013282, URL [http://doi.wiley.
416 com/10.1002/2017JC013282](http://doi.wiley.com/10.1002/2017JC013282).

LIST OF FIGURES

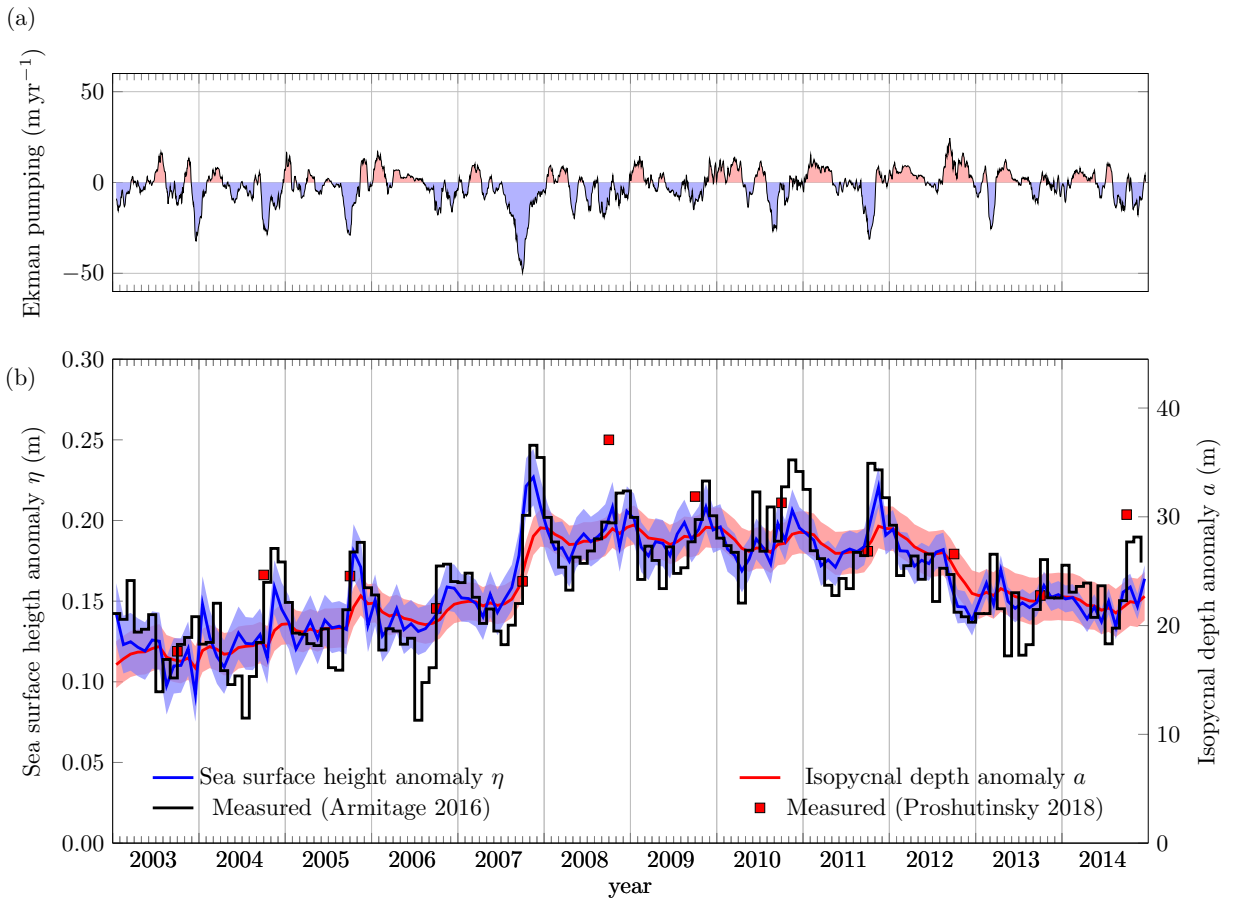
- 418 **Fig. 1.** a) The doming of satellite-derived Dynamic Ocean Topography (DOT) marks the persistent
419 anticyclonic circulation the Beaufort Gyre, one of the main features of the Arctic Ocean
420 (color, 2003-2014 mean, data from Armitage et al. (2016)). The white area is beyond the
421 81.5°N latitudinal limit of the Envisat satellite. The Beaufort Gyre Region used for com-
422 putations in this study, including only locations within $70.5^\circ - 80.5^\circ\text{N}$ and $170^\circ - 130^\circ\text{W}$
423 whose depth is greater than 300 m, is marked by the thick red line. b) A section across the
424 Beaufort Gyre Region at 75°N , marked by a dashed line in (a), shows how the doming up
425 of the sea surface height toward the middle of the gyre is reflected in the bowing down of
426 isopycnals. The stratification is dominated by salinity variations and concentrated close to
427 the surface, with potential densities ranging from a mean value of 1021 kg m^{-3} at the surface
428 to close to 1028 kg m^{-3} at a depth of about 200 m, and remaining almost constant below that. 23
- 429 **Fig. 2.** Schematic of the idealized two-layer model: the wind- and ice-driven Ekman flow (blue)
430 drives variations in the layer thicknesses or, equivalently, in the sea surface height η and
431 isopycnal depth a . The interior is assumed to be in geostrophic balance, and eddy processes
432 (red) result in a volume flux flattening the isopycnal slope. 24
- 433 **Fig. 3.** Observations of monthly mean Ekman pumping (black, top panel) and mean sea surface
434 height anomaly (black, bottom panel) over the Beaufort Gyre Region are assimilated in
435 the idealized model (1). Blue and red filled areas in the top panel denotes upwelling and
436 downwelling respectively. Red marks shows the 30 psu isohaline depth anomaly estimated
437 from hydrographic data for August-September-October of each year (Proshutinsky et al.
438 2009); in the Arctic, isohaline depth can be considered a good approximation to isopycnal
439 depth because the ocean stratification is mostly due to salinity variations. The estimated
440 sea surface height anomaly (blue), isopycnal depth anomaly (red), eddy diffusivity $K =$
441 $218\text{ m}^2\text{ s}^{-1}$ and reduced gravity $g' = 0.065\text{ m s}^{-2}$ (corresponding to $\Delta\rho = 6.8\text{ kg m}^{-3}$) are in
442 agreement with observations. In particular, the estimated sea surface height anomaly (blue)
443 captures most of the observed seasonal cycle variability (black) as well as its long-term
444 increase after 2007 (RMSE = 0.02 m, $R^2 = 0.68$). The estimated bottom Ekman layer
445 thickness is $d = 58\text{ m}$, and includes the effects of bottom bathymetry. Shaded blue and red
446 regions in the bottom panel show the uncertainty of the model estimation (one standard
447 deviation). 25
- 448 **Fig. 4.** a) Ekman pumping associated with wind forcing w_a (dark blue) ice forcing w_{i0} (light blue),
449 eddy fluxes $K \frac{a}{L^2}$ (dark red) and the Ice-Ocean governor w_{ig} (light red). See equation (4). The
450 mean Ice-Ocean governor term w_{ig} is six times larger than the mean eddy fluxes term Ka/L^2 .
451 b) hypothetical isopycnal depth anomaly under different scenarios: red line and red marks
452 are the same as in Figure 3b, with the red shaded region denoting one standard deviation.
453 The orange curve represents the evolution of the isopycnal obtained by neglecting eddy
454 diffusivity in equation (1). The blue curve is obtained by neglecting the ice-ocean governor.
455 The error introduced by not including the ice-ocean governor is much larger (gray arrows),
456 with an increase in isopycnal depth anomaly more than ten times larger the actual one over
457 the 12-year period considered. 26



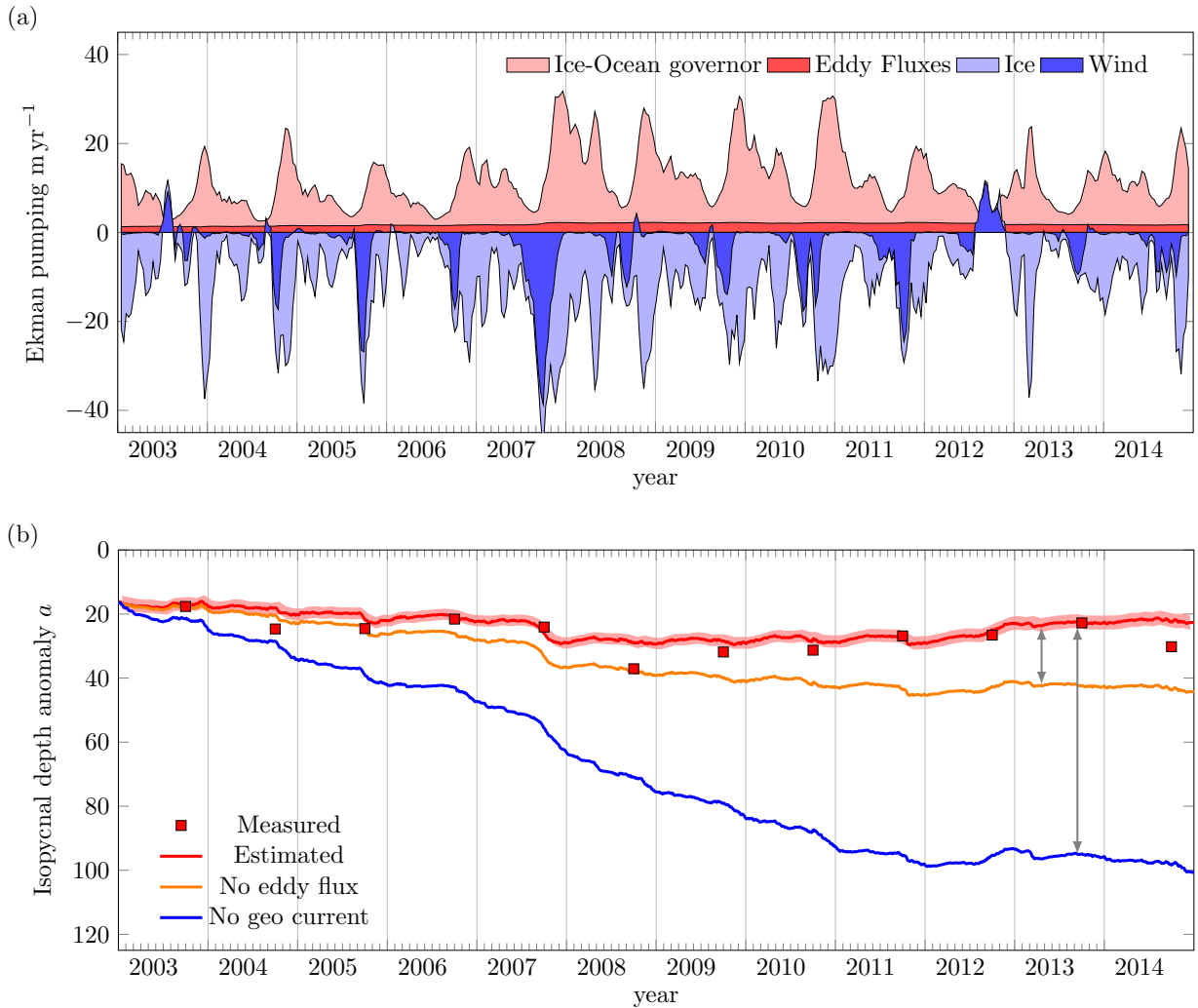
458 FIG. 1. a) The doming of satellite-derived Dynamic Ocean Topography (DOT) marks the persistent anticy-
 459 clonic circulation the Beaufort Gyre, one of the main features of the Arctic Ocean (color, 2003-2014 mean, data
 460 from Armitage et al. (2016)). The white area is beyond the 81.5°N latitudinal limit of the Envisat satellite. The
 461 Beaufort Gyre Region used for computations in this study, including only locations within 70.5° – 80.5°N and
 462 170° – 130°W whose depth is greater than 300 m, is marked by the thick red line. b) A section across the Beau-
 463 fort Gyre Region at 75°N, marked by a dashed line in (a), shows how the doming up of the sea surface height
 464 toward the middle of the gyre is reflected in the bowing down of isopycnals. The stratification is dominated
 465 by salinity variations and concentrated close to the surface, with potential densities ranging from a mean value
 466 of 1021 kg m^{-3} at the surface to close to 1028 kg m^{-3} at a depth of about 200 m, and remaining almost constant
 467 below that.



468 FIG. 2. Schematic of the idealized two-layer model: the wind- and ice-driven Ekman flow (blue) drives
 469 variations in the layer thicknesses or, equivalently, in the sea surface height η and isopycnal depth a . The
 470 interior is assumed to be in geostrophic balance, and eddy processes (red) result in a volume flux flattening the
 471 isopycnal slope.



472 FIG. 3. Observations of monthly mean Ekman pumping (black, top panel) and mean sea surface height
 473 anomaly (black, bottom panel) over the Beaufort Gyre Region are assimilated in the idealized model (1). Blue
 474 and red filled areas in the top panel denotes upwelling and downwelling respectively. Red marks shows the
 475 30 psu isohaline depth anomaly estimated from hydrographic data for August-September-October of each year
 476 (Proshutinsky et al. 2009); in the Arctic, isohaline depth can be considered a good approximation to isopyc-
 477 nal depth because the ocean stratification is mostly due to salinity variations. The estimated sea surface
 478 height anomaly (blue), isopycnal depth anomaly (red), eddy diffusivity $K = 218 \text{m}^2 \text{s}^{-1}$ and reduced gravity
 479 $g' = 0.065 \text{ms}^{-2}$ (corresponding to $\Delta\rho = 6.8 \text{kg m}^{-3}$) are in agreement with observations. In particular, the esti-
 480 mated sea surface height anomaly (blue) captures most of the observed seasonal cycle variability (black) as well
 481 as its long-term increase after 2007 ($\text{RMSE} = 0.02 \text{m}$, $R^2 = 0.68$). The estimated bottom Ekman layer thickness
 482 is $d = 58 \text{m}$, and includes the effects of bottom bathymetry. Shaded blue and red regions in the bottom panel
 483 show the uncertainty of the model estimation (one standard deviation).



484 FIG. 4. a) Ekman pumping associated with wind forcing w_a (dark blue) ice forcing w_{i0} (light blue), eddy
 485 fluxes $K \frac{a}{L^2}$ (dark red) and the Ice-Ocean governor w_{ig} (light red). See equation (4). The mean Ice-Ocean
 486 governor term w_{ig} is six times larger than the mean eddy fluxes term Ka/L^2 . b) hypothetical isopycnal depth
 487 anomaly under different scenarios: red line and red marks are the same as in Figure 3b, with the red shaded
 488 region denoting one standard deviation. The orange curve represents the evolution of the isopycnal obtained by
 489 neglecting eddy diffusivity in equation (1). The blue curve is obtained by neglecting the ice-ocean governor.
 490 The error introduced by not including the ice-ocean governor is much larger (gray arrows), with an increase in
 491 isopycnal depth anomaly more than ten times larger the actual one over the 12-year period considered.